Experimental investigation on thermomechanical properties and micro-machinability of carbon nanofibre reinforced epoxy nanocomposites

Bao Le [a], Guoyu Fu [b], Jibran Khaliq [c], Dehong Huo [b,*], Islam Shyha [a,d]

[a] *School of Computing, Engineering and the Built Environment, Edinburgh Napier University, EH10 5DT Edinburgh, UK*
[b] *Mechanical Engineering, School of Engineering, Newcastle University, NE1 7RU Newcastle upon Tyne, UK*
[c] *Mechanical and Construction Engineering Department, Northumbria University at Newcastle, NE1 8ST Newcastle upon Tyne, UK*
[d] *Production Engineering Department, Faculty of Engineering, Alexandria University, Alexandria 21544, Egypt*

A B S T R A C T

A comprehensive experimental investigation on thermomechanical properties and micro-machinability of carbon nanofibre reinforced epoxy nanocomposites (EP/CNF) is presented in this study. The machinability indicators including cutting force and surface roughness have been investigated. Tensile properties, morphology of tensile fracture surfaces, glass transition temperature, machined chip morphology, and machined surface morphology were also characterised. To investigate the effect of both workpiece material properties and operating conditions on the machinability of EP/CNF, three controlled quantitative factors were selected at different levels, namely CNF loading, cutting speed and feed per tooth (FPT). Micromilling experiments were performed on an ultra-precision desktop micro-machine tool using titanium-carbon-nitride (TiCN) coated micro-end mills. Among all compositions with CNF concentration ranging from 0.3 to 1 wt%, EP/1 wt% CNF exhibited the best machinability among other nanocomposites with its lowest cutting force of approximately 0.5 N and surface roughness of 0.18 μm. Size effect appeared at FPT below minimum uncut chip thickness (MUCT) indicated by the strong deterioration of surface quality owing to the dominant ploughing effect.

1. Introduction

Carbon nanofibres (CNFs) can be defined as sp^2-based linear filaments [1]. Their diameters can be in the range of 50–500 nm with lengths around a few tens of micron, giving these fibres high aspect ratios of length/diameter (>100) [2]. CNFs can be distinguished from other carbon fibres or carbon nanotubes (CNTs) with their typical structure such as regular stacked, truncated conical or planar layers [3–5], as shown in Fig. 1. Due to their high aspect ratio combined with excellent mechanical and physical properties such as Young's modulus ~500 GPa, tensile strength ~3 GPa, electrical conductivity ~10^3 S/cm, thermal conductivity ~1900 W m^{-1} K^{-1}, CNFs show great potential as reinforcing fillers in polymer nanocomposites [6].

Following the new demand of modern manufacturing in miniaturising products/components to optimise working efficiency as well as producing micro-components in various applications such as electronics, and medical [7], polymer composites have shown great potential as structural materials such as micro-gears [8], micro-robotic cell transporters (MCTs) [9], micro-pillars [10], or micro-transporters [11].

Although many methods such as micro-moulding, lithography, or 3D printing have been employed to manufacture these micro-parts, mechanical micromachining techniques like micro-milling should be applied to obtain higher surface quality and dimensional accuracy. However, most of the relevant studies have been recently focusing on the mechanical and physical characterisation of pre-machined EP/CNF nanocomposites [2,7,12,13]. To the best of our knowledge, investigations of machinability of EP/CNF nanocomposites using micromachining has yet to be addressed. Therefore, this study presents a comprehensive experimental investigation on the machinability of EP/CNF nanocomposites through micromilling process taken into consideration cutting force and surface roughness as the key process indicators. Additionally, chip morphology and machined surface morphology were also investigated to support the analysis of these two main machinability indicators. To consider the effect of the workpiece materials on the micromachining performance at different filler contents, various mechanical and physical properties characterisations were also conducted before the microcutting trials.

---

2. Materials and methods

2.1. Materials

A two-component Bisphenol A-epichlorohydrin (BPA) based epoxy was used in this study. Epoxy resin (EL5) and hardener (EHA571) were supplied by Polyfibre (Birmingham, UK). CNFs (CNF-110) were provided by GNM (Las Cruces, USA) with diameters from 200 to 600 nm and lengths from 5 to 50 μm. Epoxy/CNF composites containing different weight contents (0.1 to 1.0 wt%) were prepared using a two-step method. In the first step, CNFs and epoxy hardener were hand mixed for 5 min inside the glove box to avoid any air transmission and nanofiller exposure. The hand-mixed solution was then moved out from the glove box and further mixed using ultrasonication for 10 min at room temperature to attain a homogenous mixture. To avoid over-heating that can cause damage to the nanofibres, an ice bath was used to cover outside the beaker and the sonication was performed at 60 % of the maximum power (643 W) at a frequency of 250 kHz. Moreover, a setting with a five-second break was applied after each ten-second operation. After obtaining a homogeneous mixture, epoxy resin was added to this solution using hand mixing for 5 min. The final solution was degassed in a vacuum chamber at room temperature before moulding. The samples were cured at room temperature for 24 h followed by oven curing at 80 °C for 2 h for full crosslinking of EP. The fabrication process of EP/CNF nanocomposites is shown in Fig. 2.

2.2. Thermomechanical characterisation of EP/CNF nanocomposites

Tensile tests were performed on a Universal Testing Machine (INSTRON 3382) based on ASTM standard D638. Type V specimens with dimensions 63.5 × 9.53 × 4 mm (L × W × B) were used. Five specimens were used for each composition with a displacement rate of 0.5 mm/min. The morphology of these tensile fracture surfaces was also investigated using a scanning electron microscope (SEM) (TESCAN MIRA3) to identify failure patterns and fibre distribution.

Dynamic Mechanical Analyzer (DMA) (Model 8000, Perkin Elmer) was used to identify the glass transition temperature Tg of EP/CNF nanocomposites. The details of DMA testing parameters are indicated in Table 1.

2.3. Micromachining experiments

An ultra-precision desktop micro-machine tool (Nanowave MTS5R) was employed to perform micromilling experiments in this study. High-speed cutting in micromachining was generated by a high-speed spindle driven by a power of 100 W (240 V) that can reach 80,000 rpm. Also, an air spindle was used to minimise cutting vibration. The high rigidity of the machine base also helps the machine tool reach a high resolution of 0.1 μm. Full immersion micro-milling was applied for all cutting trials in dry condition. The experimental setting is shown in Table 2. The setup is shown in Fig. 3 which includes the nanocomposite specimen, the main spindle, the micro-end mill and the dynamometer.

A piezoelectric dynamometer (Kistler 9256C2) with high frequency (up to 4.8 kHz) was attached behind the fixture to measure the micro-cutting forces. Kistler 5070A multichannel charge amplifier and Kistler 5697A1 DAQ with Dynoware software were used for signal processing and data acquisition. Surface roughness Ra measurements were performed on an Alicona Infinite Focus G4 at the central line of the machined slot. Average values were obtained from five measurements at different positions (entry, middle, and exit) in the feed direction. The surface roughness Ra was also measured using Mitutoyo Surftest SJ-410 (0.25 mm and 2.5 mm cut-off and measurement length, respectively) (Figure 3.20) at the centre line of each slot. Average values were similar to those of Alicona Ra measurements. These Ra measurements were used to validate the results from the contactless method (using the Alicona microscope).

3. Results and discussion

3.1. Microstructural analysis of tensile fracture surfaces

The analysis of the fractured surfaces was performed to investigate the toughening mechanisms as well as filler distribution when adding different CNT loadings into the epoxy matrix (Fig. 4). Generally, the fracture samples showed a river-like pattern of radiating crack lines, regardless of the filler contents that indicated a typical failure pattern of
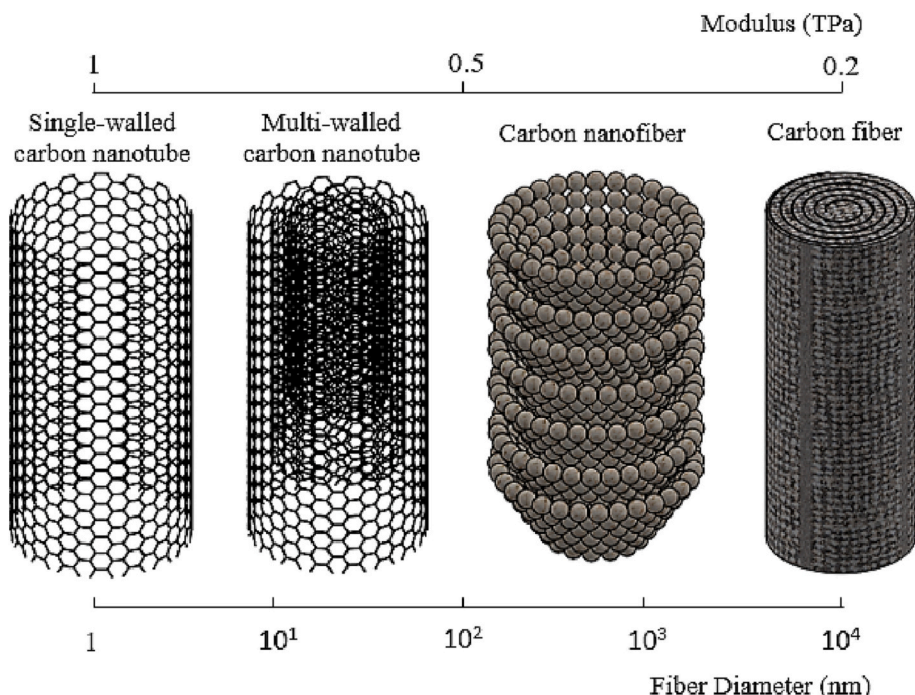
Fig. 1. Various types of fibrous carbon materials from nano to microscale.
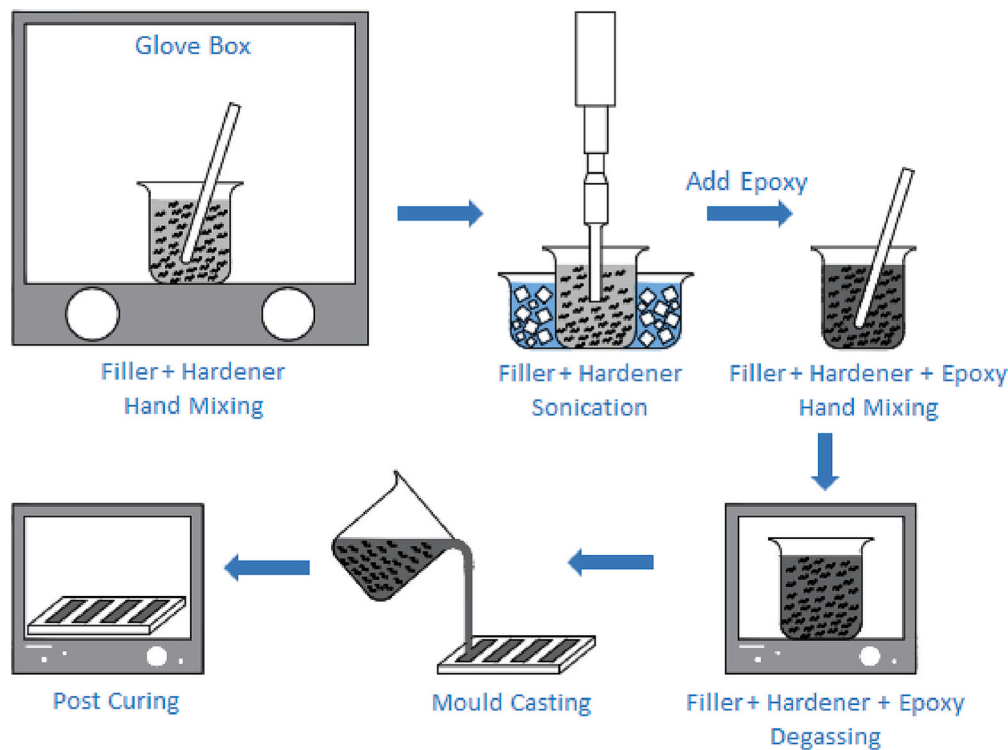
Fig. 2. Schematic shows the fabrication of EP/CNF nanocomposites.

Table 1
DMA testing parameters.

Specimen (L × W × T)	20 × 5 × 1 (mm)
Test mode	Single cantilever
Test frequency	1 Hz
Oscillation amplitude	0.05 % strain
Initial temperature	45 °C
Heating rate	Ramp 5 °C/min to 150 °C
Preload	0.01

Table 2
Experimental settings.

Specimen	Material	CNF reinforced epoxy and plain epoxy
	Dimension (L × W × T) (mm³)	70 × 13 × 3
	Filler loading (wt%)	0, 0.1, 0.3, 0.7 and 1
Cutting tool	Material	Titanium-carbon-nitride (TiCN) coated micro-end mills
	Number of flutes	2
	Flute length (mm)	1.5
	Cutting diameter (mm)	0.5
	Helix angle	20°
Cutting conditions	Cutting speed (m/min)	31.41, 78.54 and 125.67
	Feed per tooth (μm)	0.2, 0.5, 1, 2, 5
	Axial depth of cut (DoC) (μm)	100
	Cutting width (μm)	0.5
	Cutting length (mm)	13

brittle materials. However, a gradual change from rough and irregularly dendritic (Fig. 6a, b, and e) to smooth and radially straight cracks (Fig. 4c and d) could be observed when more CNF was added. It indicated the toughening effect provided by CNF additions that restricted the free crack propagation (as could be seen in neat epoxy samples).

Fig. 5 shows the tensile fracture surfaces of epoxy/CNF nanocomposite samples at high magnification to exhibit the filler

distributions. The fracture morphology of 0.1 and 0.3 wt% nanocomposites appeared to be smooth with uniform distribution of CNFs (Fig. 5a and b). Additionally, crack spinning, and crack deflection could also be observed on the fracture surfaces of 0.1 and 0.3 wt% nanocomposites that indicated the highly efficient toughening mechanism of these materials [14]. It resulted in the improvements of fracture strain at these materials compared to the epoxy sample which was confirmed by the mechanical results from Section 3.2 (Fig. 6). On the contrary, clear CNF bundles and rough fracture surfaces were observed for 0.7 and 1.0 wt% CNF nanocomposites (Fig. 5c, d) that implied the poor distribution of the fillers at such high loadings. Additionally, coarse fracture surfaces, large crack lines, and CNF agglomerates in this high-filler-content group (Fig. 5c, d).

3.2. Mechanical properties

Fig. 6 shows the mechanical properties including tensile strength, Young's modulus, and fracture strain of epoxy/CNF nanocomposites at different CNF contents. The properties mentioned above appeared to improve with the addition of 0.1 and 0.3 wt% CNF but, they began to decline at larger filler loadings. For tensile strength (Fig. 6a), epoxy/0.1 wt% CNF outperformed epoxy/0.3 wt% CNF by 6.4 % and 5.3 %, respectively compared to neat epoxy. The enhancement was attributed to CNF fibres that could bear a fraction of the load from the epoxy matrix, hence improving the tensile strength of the nanocomposites. The degree of reinforcement, however, was determined by the dispersion of fibres inside the matrix. The more uniform distribution increased the probability of fibre-matrix interaction rather than fibre aggregation (fibre-fibre interaction).

Based on that, these homogenously dispersed CNFs could form a continuous network inside the epoxy matrix. It resulted in the efficient transfer of the tensile load from the epoxy matrix, hence improving the tensile strength of the nanocomposites [15]. However, the tensile strength started to decrease as higher filler contents were incorporated and reached the lowest value at 46.8 MPa for 1 wt% sample, nearly 28.6 % lower than neat epoxy. It was attributed to the uneven distribution of
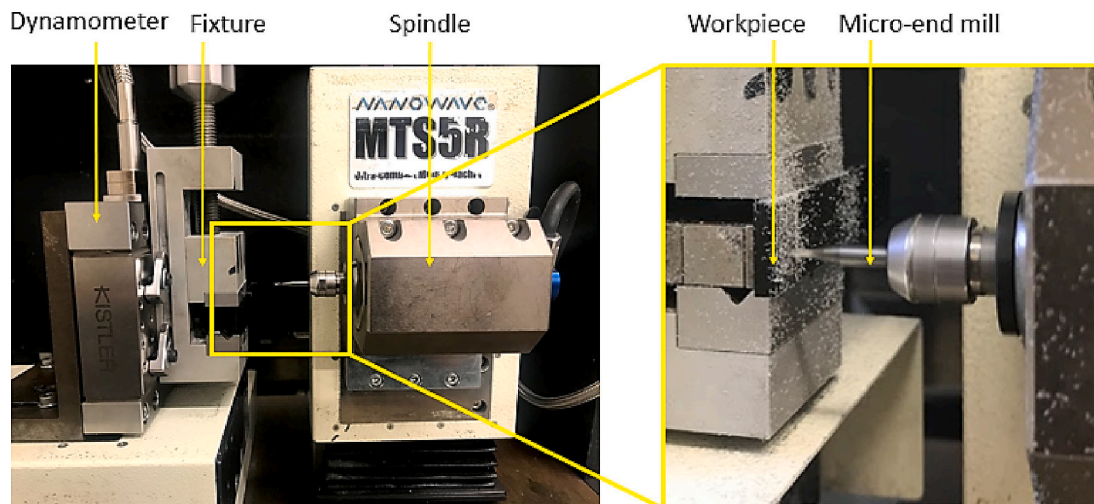
Fig. 3. Experimental setup for the micromilling trials.
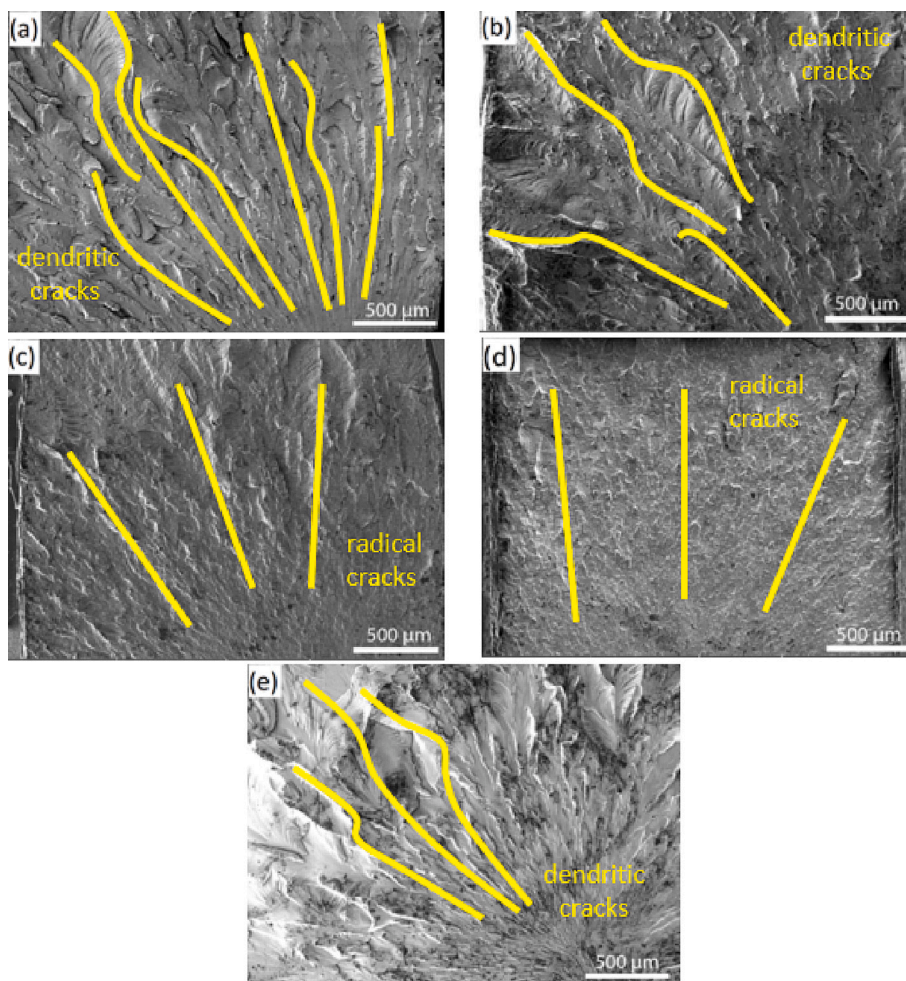
Fig. 4. SEM micrographs of the tensile fracture surfaces of (a) epoxy/0.1 wt% CNF, (b) epoxy/0.3 wt% CNF, (c) epoxy/0.7 wt% CNF, (d) epoxy/1 wt% CNF, (e) epoxy.

CNF in the epoxy matrix, indicated by more CNF agglomerates observed in Fig. 5c and d that led to the presence of the stress concentration, hence reducing the tensile strength at such high filler loadings [16,17].

Young's modulus showed a similar trend with the highest value of 1.1 GPa at 0.1 wt% and the lowest of 0.94 GPa at 1.0 wt% (Fig. 6b). This

phenomenon could also be explained by the transformation from homogenous to the inhomogeneous distribution of CNFs as their loading increased. A uniform network formed by CNF fibres at the low filler loadings (0.1 wt% and 0.3 wt%) (Fig. 5a, b) could efficiently restrain the movement of the polymer chains. As a consequence, Young's modulus or
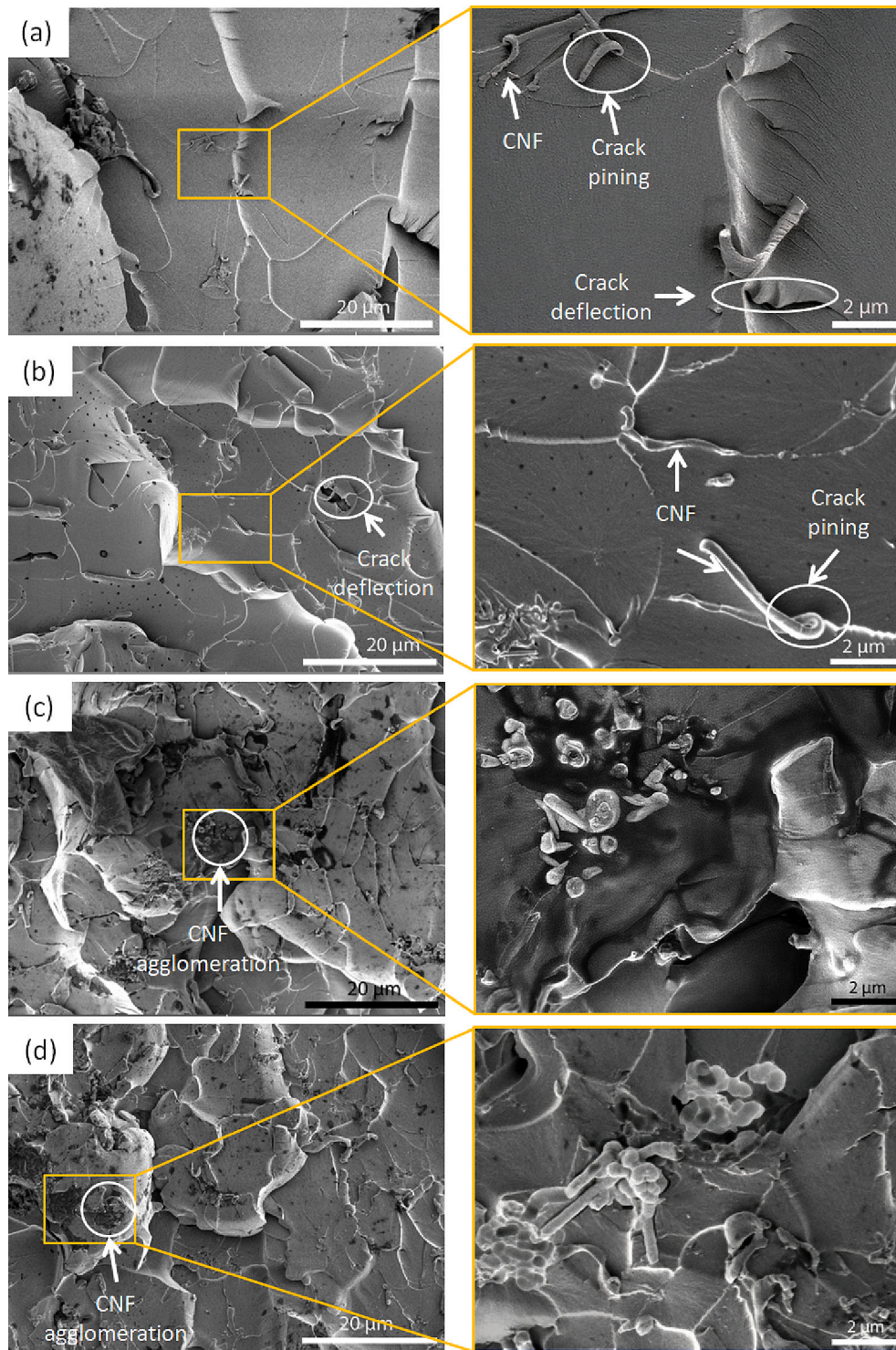
Fig. 5. SEM micrographs at high magnifications of the tensile fracture surfaces of (a) epoxy/0.1 wt% CNF, (b) epoxy/0.3 wt% CNF, (c) epoxy/0.7 wt% CNF, (d) epoxy/1 wt% CNF.

the stiffness of these materials was also enhanced [18]. Similarly, the fracture strain also showed a ductile-to-brittle transition as the filler loading increased (Fig. 6c), significantly observed at 0.7 and 1 wt% CNF due to CNF agglomeration (Fig. 5c and d) that caused stress concentration. The well-dispersed CNF nano-fibres at low filler contents appeared to improve the fracture strain of the nanocomposites [17].

3.3. Glass transition temperature

Fig. 7 illustrates a typical variation of epoxy/CNF nanocomposites' tan δ (ratio of loss modulus to storage modulus) as a function of temperature. The average glass transition temperature was identified based on the peak values of tan δ and is shown in Table 3. The gradual growth of the glass transition temperature at low filler was observed which reached the peak of 70.6 °C at 0.3 wt% CNF. Tg dropped for the filler content above 0.3 wt%. The homogenous distribution of CNF at 0.1 and
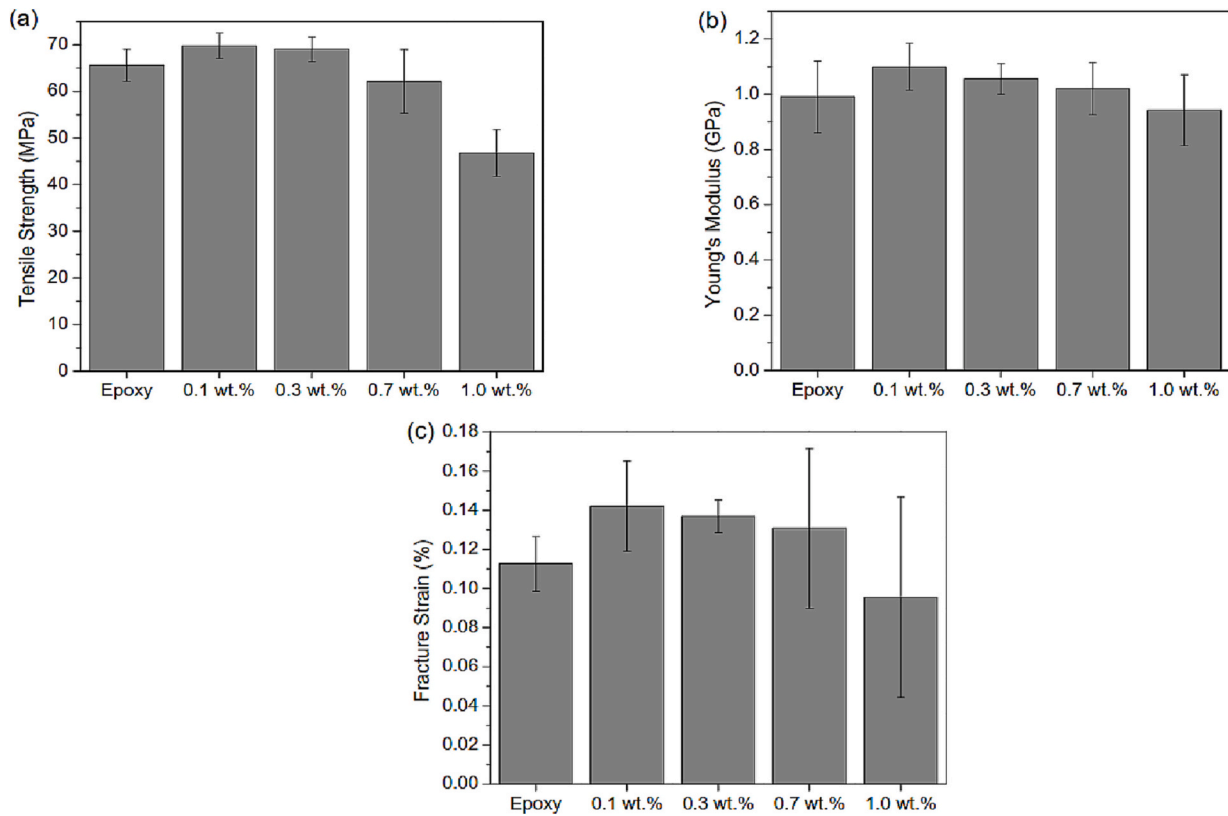
Fig. 6. Tensile properties of epoxy/CNF nanocomposites at different filler contents: (a) tensile strength, (b) Young's modulus, (c) fracture strain.
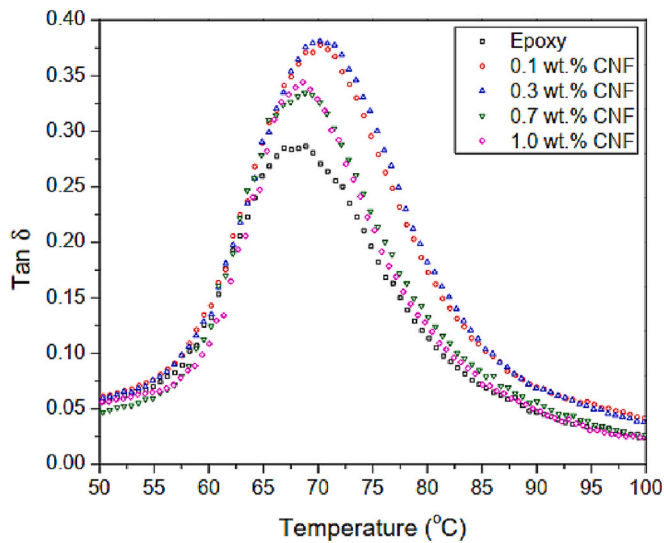
Fig. 7. Tan δ of epoxy/CNF nanocomposites at different filler contents from DMA analysis.

Table 3
Glass transition temperature of epoxy/CNF nanocomposites at different filler contents.

CNF concentration (wt%)	Glass transition temperature T_g (°C)
0	69.5 (±0.55)
0.1	70.5 (±0.47)
0.3	70.6 (±0.76)
0.7	68.7 (±0.07)
1	67.3 (±1.82)

0.3 wt% (Fig. 5a, b) contributed to their high magnitudes of Tg. It was due to the well-dispersed nano-fibres at such low contents that could form a continuous network to restrict the polymer chains' mobility or increased the immobilization of macromolecules [19], hence stabilising the material structure in response to accelerated thermal energy.

On the contrary, more agglomerations of CNFs at higher filler contents (Fig. 5c, d) led to the reduction of T_g by 3 % lower than neat epoxy at 1 wt% CNF. These aggregations of the nano-fibres resulted in less matrix-filler interaction and left the more free volume of polymer chains, hence making the polymer's structure unstable at high temperatures. The poor dispersion of nano-fillers also contributed to the degradation of the polymer's mechanical properties as it impeded the curing and reduces the crosslinking density [20]. The effect of filler concentration on the transition temperature of epoxy/CNF nanocomposites from Table 3 showed high agreement with other investigations on various polymer nanocomposites such as epoxy/graphene [18] or PU/graphene oxide (PU/GO) [21]. This finding is also in line with the tensile properties (Section 3.1) that reconfirmed the obvious effect of fillers' distribution on the thermomechanical properties of epoxy/CNF nanocomposites.

3.4. Chip morphology

Fig. 8 depicts the chip morphology for different polymer nanocomposites and neat epoxy at a cutting speed of 78.54 m/min. As a general trend, chip morphology started to change from debris/discontinuous to continuous form as FPT increased from 0.2 to 5 μm. These transition points (denoted by horizontal arrows) were supposed to be the MUCT and they depended on the mechanical properties of workpiece materials. The chips when micromilling 0.1 wt% nanocomposite (Fig. 8a) started to form from 0.2 μm of FPT which likely indicated the lowest MUCT of 0.2 μm compared to other compositions (0.3 to 1 wt%). Similarly, the MUCT of both 0.3 and 0.7 wt% CNF nanocomposites were 0.5 μm (Fig. 8b, c).
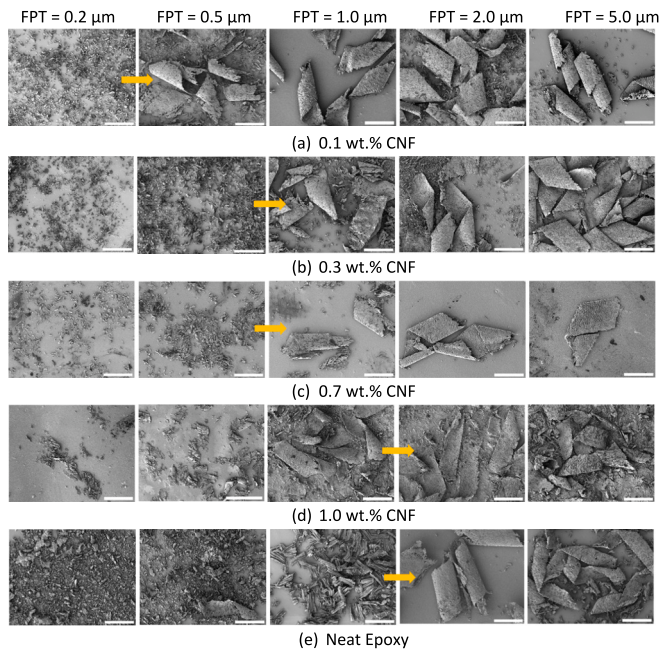
Fig. 8. Chip morphology of epoxy/CNF nanocomposites at different filler contents (cutting speed = 78.54 m/min) (scale bar is 200 μm).

The highest value of the MUCT was observed at 1 wt% CNF and neat epoxy of 1 μm (Fig. 8d, e). The reduction of MUCT as the filler content increased was likely due to the enhancement of the ductility. Based on the tensile property results detailed in Section 3.2, the addition of 0.1 wt % CNF provided the highest improvement of the fracture strain, followed by 0.3 and 0.7 wt%. However, there was a ductile-to-brittle transition as the filler content reached 1 wt% (Fig. 6c).

This ductile-to-brittle transition of 1 wt% nanocomposite and epoxy led to the chip formation only at higher FPT or higher MUCT compared to those of ductile nanocomposites (0.1, 0.3, and 0.7 wt%). On closer observation of chip morphology, Fig. 9 illustrates the effect of FPT and filler content on the chip morphology at 78.54 m/min cutting speed. The chip surface appeared to be coarser at high feed rates as the FPT increases. The broad shear zone at high feed rates made the chip segments larger hence roughening the chip surfaces. The chip morphology showed a clear difference between various nanocomposites and epoxy at FPT of 1 μm. At this FPT, the chip thickness was low and likely to be deformed due to the heat generated from the cutting process and physical cutting force. Therefore, the chip formation, in this case, was affected by the thermomechanical properties of the workpiece materials. The well-enhanced thermomechanical properties of 0.1 and 0.3 wt% CNF nanocomposites exhibited high integrity chip formation with flat and smooth surfaces and fewer cracks at FPT of 1 μm (Fig. 9a, b) compared to other compositions (i.e., 0.7 and 1 wt% and epoxy). Moreover, the chips at 1 wt% and epoxy appeared to be wrinkled (Fig. 9d, e), especially for epoxy (Fig. 9e). This was due to the thermal softening at the high cutting speed that was attributed to the low transition temperature of these nanocomposites (Table 3).

3.5. Cutting force

ANOVA analysis was applied to statistically identify the importance of input factors. Table 4 presents ANOVA results for the resultant cutting force that analysed the impact of three main input factors. Although, filler content, FPT, and cutting speed were found statistically significant on cutting force, cutting speed was found the most significant factor affecting the cutting force with a contribution of 74.5 %.

Fig. 10 shows variation in cutting force as a function of cutting speeds (from 31.41 to 125.67 m/min) and FPT. Generally, cutting force gradually increased along with FPT regardless of the workpiece materials. It implied the significant effect of FPT on cutting force. The increase of FPT provided more chip load acting on the cutting tool, leading to more resistance of workpiece material against the cutting path, and consequently, high cutting forces generated [22].

At high cutting speeds, cutting forces for 1 wt% CNF nanocomposite and epoxy samples fluctuated at the low range of FPT (0.2–2 μm) at 78.54 m/min (Fig. 10b) and 125.67 m/min (Fig. 10c). This phenomenon indicated the effect of MUCT on cutting force variation at high cutting speeds as evidence of the dominance of the size effect. As discussed in Section 3.4 1 wt% CNF nanocomposites and epoxy showed the highest MUCT (from 1 to 2 μm). It led to the occurrence of the ploughing effect at the FPT below 2 μm, resulting in the high cutting force at the FPT of 0.2 μm. Cutting force decreased with the FPT (up to 1 μm) due to the reduction of the ploughing mechanism. Due to the dominance of the shearing effect at higher FPT (from 1 to 2 μm), the cutting force increased because of the increased chip load. On the contrary, cutting force at 0.1, 0.3, and 0.7 wt% CNF exhibited a gradual rise throughout this range of FPT (0.2 to 2 μm), see Fig. 10b and c. It could be interpreted by considering the fracture strain and Young's modulus of the workpiece materials. As shown in Fig. 6b and c, both fracture strain and Young's modulus of 0.1, 0.3, and 0.7 wt% nanocomposites were higher than epoxy and 1 wt% composition. This resulted in the higher resistance of the workpiece against the tool advance at higher cutting speeds (78.54 and 125.67 m/min), hence leading to the linear raise of cutting force at FPT from 0.2 to 1 μm. The rising portion of cutting force variation at higher feed rates (2 to 5 μm) for all compositions were attributed to the increased chip load and shear area or larger plastic deformation [22,23].

From Fig. 10, it can be seen an obvious effect of filler content on cutting force, exhibited by the highest cutting force possessed by 0.1 wt % sample and decreased as the CNF percentage increased. Also, the neat epoxy sample showed the smallest magnitudes at all cutting conditions compared to its nanocomposite counterparts. It was likely to imply the considerable effect of the thermomechanical properties of materials. With the incorporation of CNFs, the epoxy-based nanocomposites showed higher cutting force magnitudes than epoxy due to the strengthening effect. From Fig. 10a–c, it appeared that the cutting force for 0.1 wt% CNF nanocomposite were at the highest values, followed by 0.3 wt% counterparts. This could be attributed to the improvements of Young's modulus (Fig. 6b) and the failure strain (Fig. 6c), owing to the uniform distribution of nano-fibres (Fig. 5a, b) of these materials. On the contrary, the low cutting forces when micromilling high-filler-content nanocomposites (0.7 and 1 wt% CNF) were contributed by the low mechanical properties compared to 0.1 and 0.3 wt% CNF due to the agglomeration of the nano-fibres (Fig. 5c, d). Also, 0.1 wt% nanocomposites exhibited significantly high cutting force magnitudes at the highest cutting speed of 125.67 m/min that was distinct from those of other compositions. At such high cutting speed, the thermal softening effect seemed to appear due to high heat generated from the cutting area. The high cutting force magnitudes when micromilling 0.1 wt% nanocomposite were due to its high thermal stability that was contributed by the high glass transition temperature of this composition (Table 3). It resulted in the stability of the mechanical properties of this material at a high cutting speed, hence increasing the cutting force.

The effect of mechanical properties of the nanocomposite workpieces and feed per tooth effect on the cutting force can be also theoretical analysed based on the equations [24] that describe the elemental cutting forces in the tool coordinate system (Fig. 11) as follows:

$$\begin{aligned} dF_t &= (k_{tc}h + k_{te})dz \\ \boldsymbol{dF_r} &= (\boldsymbol{k_{rc}h + k_{re}})\boldsymbol{dz} \\ dF_a &= (k_{ac}h + k_{ae})dz \end{aligned} \tag{1}$$

where: dF_t, dF_r, dF_a — tangential, radial, and axial element cutting forces, respectively k_{tc}, k_{rc}, k_{ac} — tangential, radial, and axial cutting coefficients, respectively k_{te}, k_{re}, k_{ae} — tangential, radial, and axial edge

FPT = 1 µm   FPT = 2 µm   FPT = 5 µm

(a) 0.1 wt.% CNF

(b) 0.3 wt.% CNF

(c) 0.7 wt.% CNF

(d) 1.0 wt.% CNF
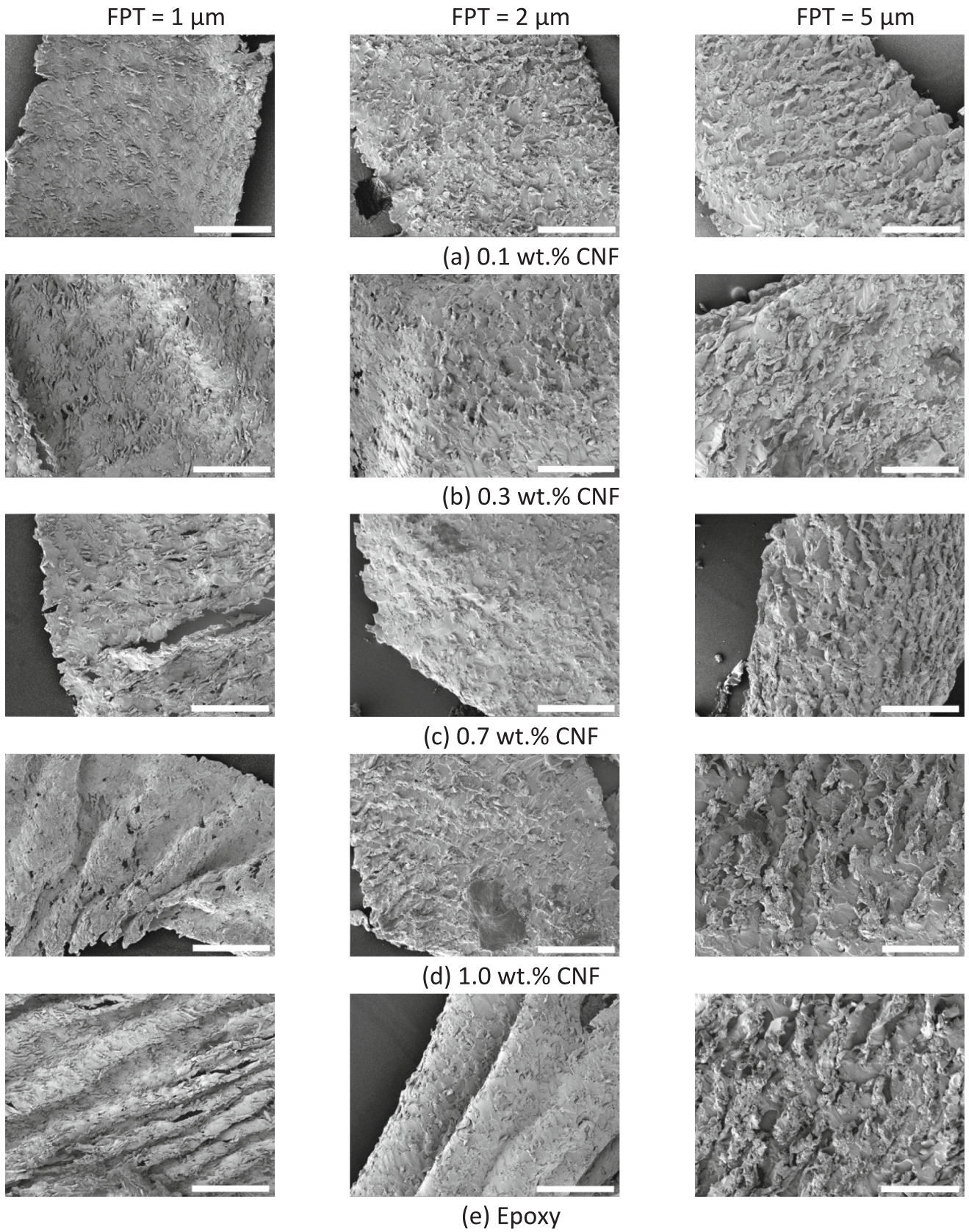
(e) Epoxy

Fig. 9. Chip morphology of epoxy/CNF nanocomposites at different filler contents (cutting speed = 78.54 m/min) (scale bar is 50 µm).

Table 4
ANOVA results for the resultant cutting force when micromilling epoxy/CNF nanocomposites.

Source	DF	Seq SS	Contribution	Adj SS	Adj MS	F-value	P-value
Filler content	4	2.146	11.09 %	2.146	0.53641	33.75	<0.001
Cutting speed	2	14.426	74.53 %	14.426	7.21316	453.86	<0.001
FPT	4	1.766	9.12 %	1.766	0.44154	27.78	<0.001
Error	64	1.017	5.26 %	1.017	0.01589		
Total	74	19.355	100.00 %				
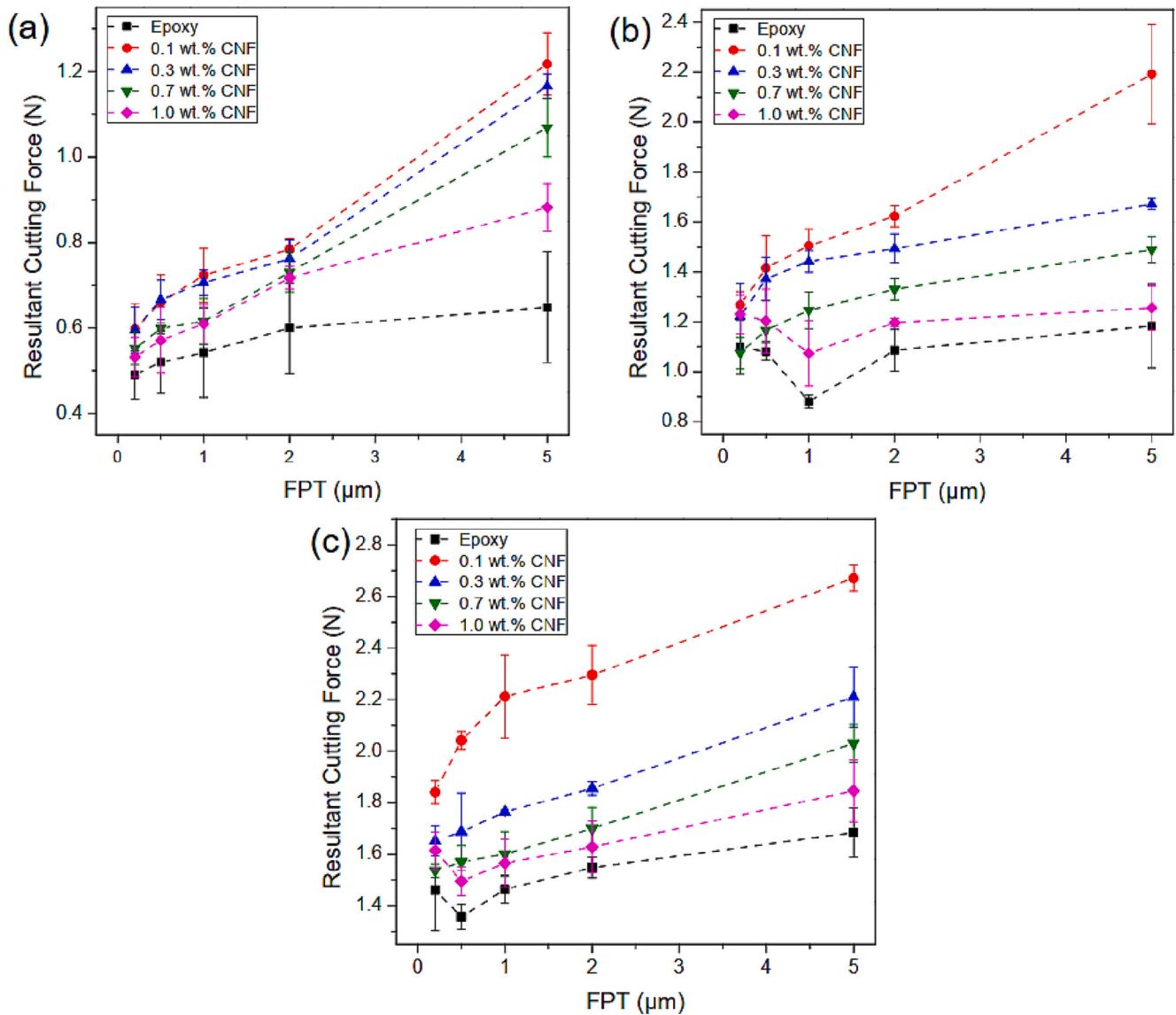
Fig. 10. Cutting force when micromilling epoxy/CNF nanocomposites at different cutting speeds: (a) 31.41 m/min, (b) 78.54 m/min, and (c) 125.67 m/min.

coefficients, respectively$h$ — chip thicknessd_z — differential axial depth of cut.

The chip thickness h from Eq. (1) can be identified based on the model developed by Jun et al. [26] that considers the effect of elastic recovery. Fig. 12 depicts the surface generation and chip thickness computation for an arbitrary axial slice in the presence of elastic recovery, which is denoted by the shaded zone, for an arbitrary axial slice. Points C and F are the tool centre and cutting edge locations, respectively. Point I is the intersection between CF and the previous surface profile. The tooth pass number is indicated by the superscript, while the rotating angle is shown by the subscript. The chip thickness is identified as follow:

$$\boldsymbol{h} = max\left(\boldsymbol{0}, \left\|\boldsymbol{C}_i^j\boldsymbol{F}_i^j\right\| - \left\|\boldsymbol{C}_i^j\boldsymbol{I}_i^{j-1}\right\|\right) \tag{2}$$

From Fig. 12, the chip thickness h value is a sum of FPT (DG) and the height of the elastic recovery height h_{er}. Therefore, increasing FPT leads to the increase of chip thickness that subsequently results in higher cutting force that was shown by the experimental results from Fig. 10. In terms of elastic recovery height h_{er}, it has been indicated that higher nanofiller content results in lower fracture strain of polymer nanocomposites [27,28], hence decreases the elastic recovery of workpiece materials or h_{er} and consequently reduces the chip thickness in micro-end milling. In this study, the fracture strain results from Fig. 6
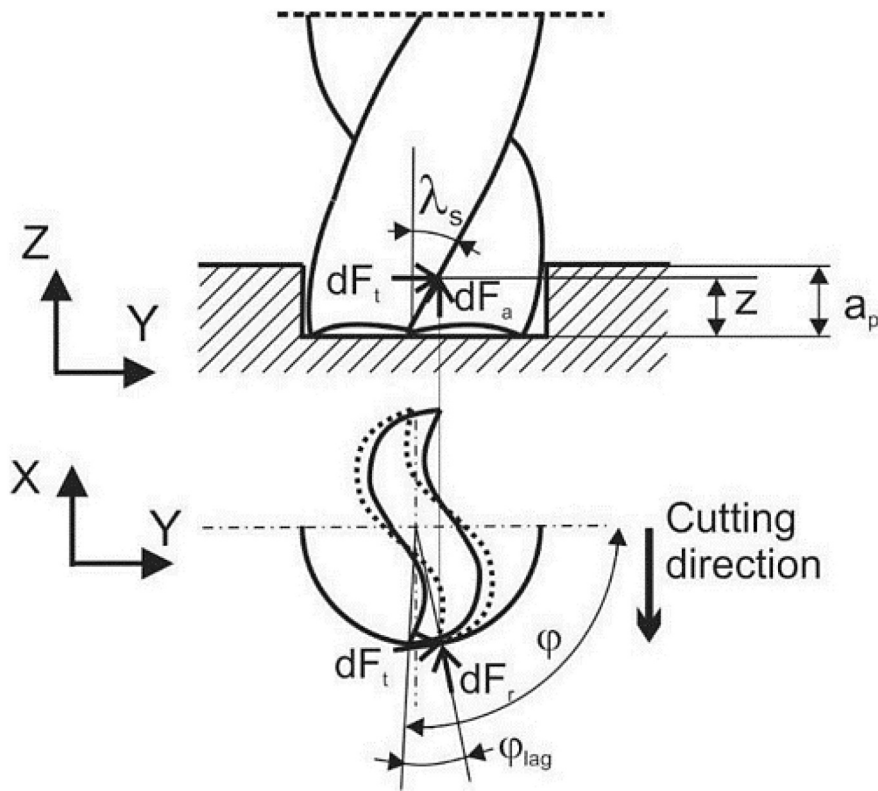
Fig. 11. Elemental forces in micro end milling [25].
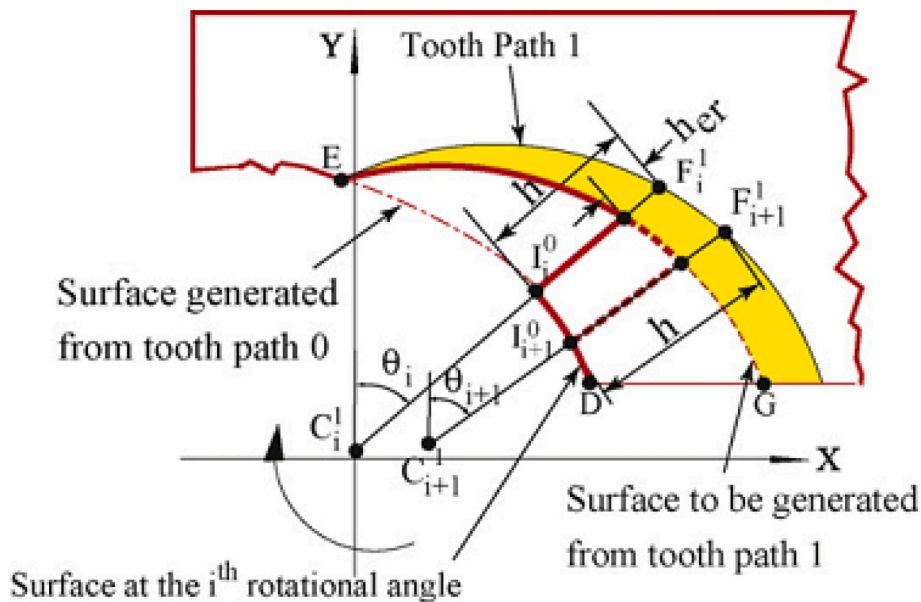
Fig. 12. Chip thickness model considering the effect of elastic recovery [26].

indicated an enhancement of the fracture strain at 0.1 wt% but gradually decreased at higher CNF concentrations. This ductile-to-brittle transition led to lower chip thickness generated when micro-milling more brittles materials (i.e., epoxy, 1 wt%), resulted in lower cutting forces as the CNF concentration increased.

3.6. Machined surface morphology

SEM images for the machined surface following the micromilling of epoxy/CNF nanocomposites and epoxy at a cutting speed of 125.67 m/min are shown in Fig. 13. SEM imaging has been performed in the middle area of the machined slot. Generally, the feed marks became clearer as the FPT increased, regardless of the material compositions Among different compositions, 0.1 wt% nanocomposites samples (Fig. 13a) had clear feed marks, even at the low FPT (0.5 μm). It was attributed to the high MUCT of this material, which made the shearing effect dominant at FPT of 0.5 μm, resulting in feed marks as the main pattern of surface morphology. However, feed marks appeared to be
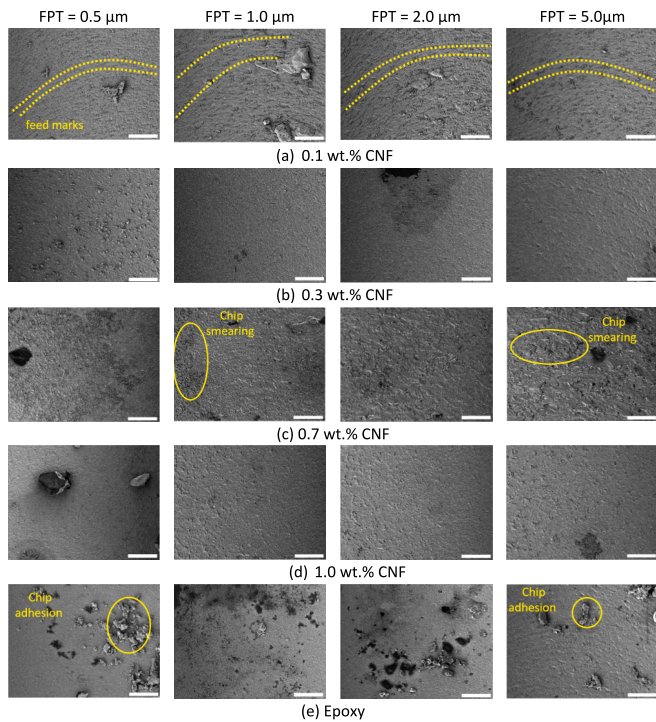
Fig. 13. SEM images of the machined surfaces when micromilling EP/CNF nanocomposites at 125.67 m/min cutting speed of (scale bar is 50 μm).

blurred at the higher filler content of 0.3 wt% CNF (Fig. 13b). As more CNF content was added, the nano-fibres appeared to be bridging the cracks along with the feed marks, hence smoothing the machined surfaces. For a further increase of filler content to 0.7 wt% CNF, the machined surface appeared to be coarse with obvious cracks covered by material adhesion (Fig. 13c). On the other hand, the machined surface of 1 wt% CNF samples (Fig. 13d) appeared to be relatively smooth that was similar to that of neat epoxy (Fig. 13e). It was attributed to the bridging and smearing effects of CNFs that smoothed the machined surfaces at such a high filler content of 1 wt% sample. This phenomenon is in line with other works with carbon nanotube (CNT) polymer nanocomposites such as EP/CNT [29] or PC/CNT [30]. The machined surface of epoxy also showed more chip adhesion at every FPT (Fig. 13e), owing to their low thermal transition temperature that consequently leads to thermal softening at high cutting speeds.

3.7. Surface roughness

Statistical analysis of ANOVA was used to identify the level of input factor distributions on the surface roughness. The results from Table 5 revealed that all filler content, FPT, and cutting speed exhibited significant effects on Ra variation. A high contribution was found at around 29 % for the filler content, followed by FPT with around 25 %. However, cutting speed appeared to show the least effect at only 9 %.

The average surface roughness of the machined surfaces exhibited a generally upward trend as FPT increased, regardless of the cutting speed and the filler content (Fig. 14). However, an initial drop in the surface

roughness could be observed at the low FPTs. Given such a low chip load, this phenomenon was attributed to the presence of ploughing at this stage due to the MUCT effect. The ploughing effect led to large compressive residual stress of the top layer of the workpiece (machined surface) [31], resulting in a highly rugged machined surface (at FPT of 0.2 μm). Due to the different MUCTs (Section 3.4), this drop portion of surface roughness varied between various compositions. For the 0.1 wt % sample, there was no drop portion in the surface roughness trend. It was due to the lowest value of MUCT possessed by this composition (0.2 μm) that resulted in a minor effect of ploughing within this FPT range. For other samples with 0.3 and 0.7 wt% CNF, the drop portion of surface roughness appeared from 0.2 to 0.5 μm FPT which was identical to their MUCT value identified from Section 3.4 (0.5 μm). Similarly for neat epoxy and 1 wt% samples with their MUCT of 1 μm and their drop portion of surface roughness stopped at FPT of 1 μm.

As the FPT exceeded the MUCT boundary, the machined surface roughness values increased with FPT (Fig. 14). This trend indicated the considerable effect of FPT on the surface roughness These results are in line with the observed feed marks at high FPTs, especially at 5 μm (Fig. 13).

Also, higher feed rates caused more plastic deformation due to higher cutting load, consequently deteriorating the machined surface quality due to increasing the high of residual area. The machined surface roughness mainly depends on the height of residual area that is identified by the geometric relationship as shown in Fig. 15 [32–34].

When FPT is larger than cutting edge radius, the height of residual area h_1 is obtained from the equation:

$$h_1 = O_2C - O_2D = r_e - \sqrt{r_e^2 - \left(\frac{f_z}{2}\right)^2}$$

$$= r_e - \sqrt{r_e^2 - \left(\frac{30v_f}{Nn}\right)^2} = r_e\left(1 - \sqrt{1 - sin^2\delta}\right) \approx r_e\frac{sin^{-1}\frac{\delta}{2}}{2} \geq \frac{f_z^2}{8r_e} \quad (3)$$

where r_e is the cutting edge radius, f_z is FPT, v_f is the feed rate of the micro end mill, N is the number of cutter flutes, n is the spindle speed, and δ is the overlapping angle of the cutting edge radius. From Eq. (3), when tool wear is neglected (corner radius r_e unchanged), the height of residual area h_1 is primarily determined by the feed per tooth f_z. Increasing FPT causes higher surface roughness, and this trend was validated by the experimental results shown in Fig. 14.

When FPT is smaller than cutting edge radius, the size effect appears. The height of residual area is identified from h_2, and MUCT t'_{min} is considered as follow:

$$h_2 = \frac{f_z^2}{8r_e} + \frac{t'_{min}}{2}\left(1 + \frac{r_e t'_{min}}{2}\right) \quad (4)$$

The theoretical value of surface roughness from Eq. (4) primarily depends on FPT f_z and the MUCT t'_{min} and validated from the experimental results shown in Fig. 14. As neat epoxy and 1 wt% CNF nanocomposite possessed the highest value of MUCT, the surface roughness of these two materials exhibited high values at low FPTs (at 0.2 μm) and rapidly decreased at higher FPTs. Similarly, this drop portion of surface roughness also appeared at 0.3 and 0.7 wt% but in a narrower range (up to 0.5 μm). For 0.1 wt% with the lowest MUCT (0.2 μm), the effect of MUCT on h_2 is negligible, and mainly depend on FPT effect like h_1, and

Table 5
ANOVA results for surface roughness when micromilling epoxy/CNF nanocomposites.

Source	DF	Seq SS	Contribution	Adj SS	Adj MS	F-value	P-value
Filler content	4	0.016096	29.21 %	0.016096	0.004024	12.82	<0.001
Cutting speed	2	0.005011	9.10 %	0.005011	0.002506	7.98	0.001
FPT	4	0.013896	25.22 %	0.013896	0.003474	11.06	<0.001
Error	64	0.020096	36.47 %	0.020096	0.000314		
Total	74	0.055100	100.00 %				
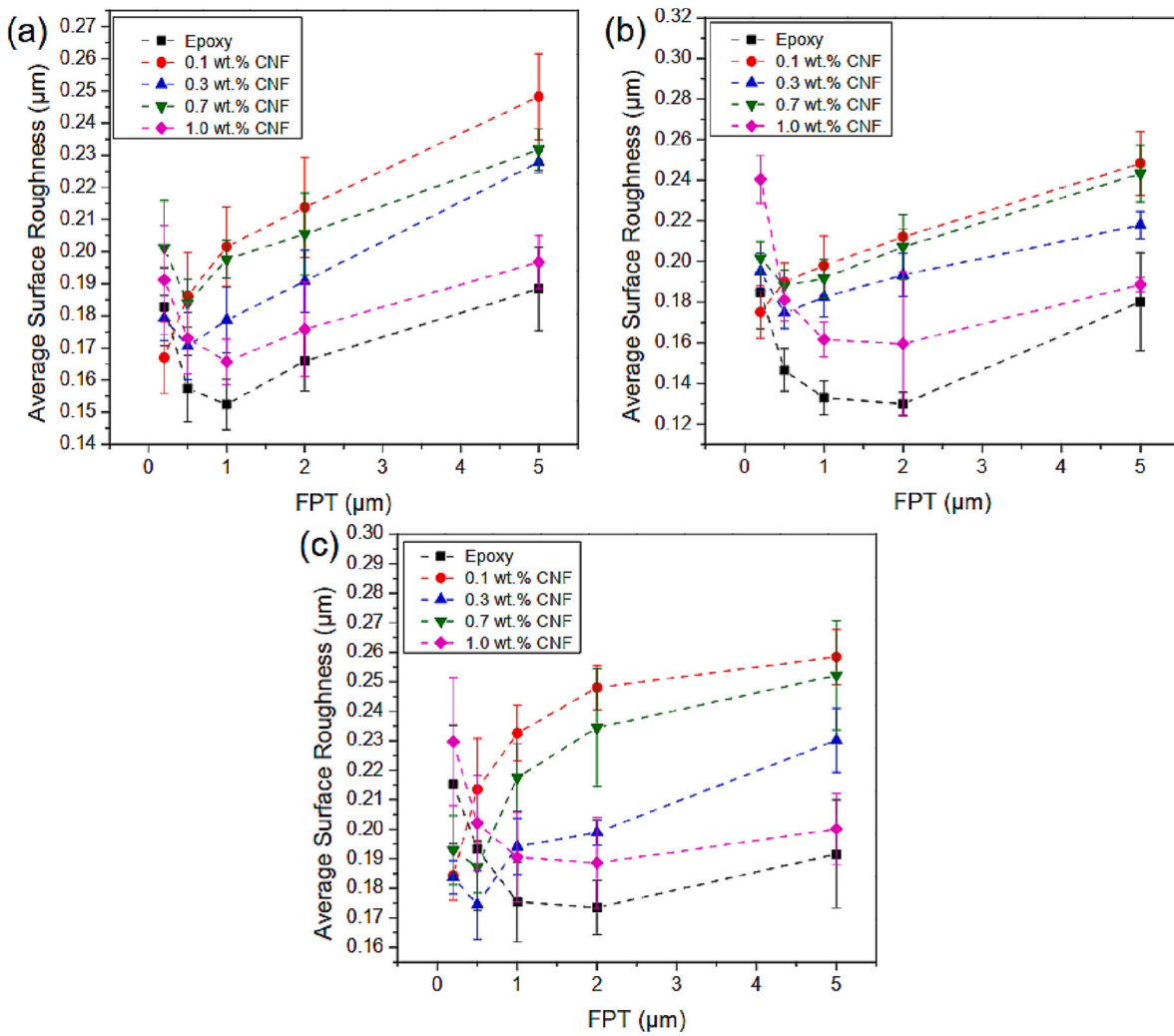
Fig. 14. Effect of the filler content and feed rate on the average surface roughness when micromilling epoxy/CNF nanocomposites at different cutting speeds: (a) 31.41 m/min, (b) 78.54 m/min, (c) 125.67 m/min.
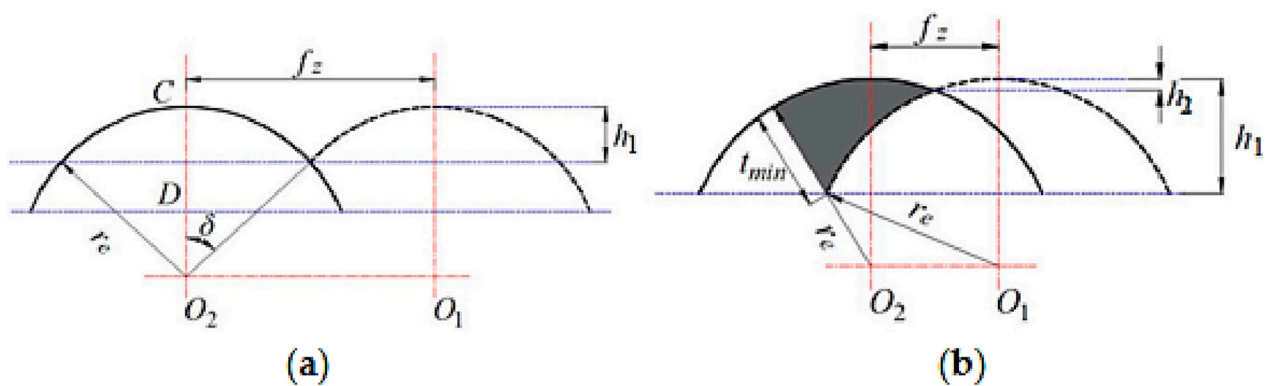
Fig. 15. Machined surface generation in micro-milling: (a) cutting edge radius is smaller than FPT, (b) cutting edge radius is larger than FPT (size effect) [34].

no drop portion of surface roughness can be seen for this material (Fig. 14).

Fig. 14 also shows the effect of filler content and subsequently, mechanical properties on the surface roughness results at the different cutting speeds despite the disorder of this trend at the lower feed rates due to the MUCT effect. Samples with 0.1 wt% CNF had the highest surface roughness values, followed by 0.7 and 0.3 wt% whereas the 1 wt

% sample had the highest surface quality among all nanocomposites. The effect of CNF concentration on surface roughness was found to be in line with the mechanical properties (Young's modulus) of different compositions (Fig. 6) that indicated the significance of the strengthening effect on surface roughness.

In addition, in micromachining, machined surface roughness possesses high sensitivity to tool vibration owing to the high cutting speed

and small tool used. This tool vibration also negatively affects the quality of the machined surface [35]. From the tensile testing results, 0.1 wt% CNF samples exhibited the highest impact of strengthening effect, owing to its high tensile strength compared to other compositions (Fig. 6). Also, this material exhibited the highest cutting forces at all cutting conditions (Fig. 10). These two factors indicated the presence of tool vibration that consequently led to the highest surface roughness of this material (Fig. 14). Similarly, this explanation can be used to support the order of Ra magnitudes for other compositions and epoxy.

The surface roughness of 0.7 wt% CNF nanocomposite samples, however, were higher than that of 0.3 wt% counterparts (Fig. 14). For 0.3 and 0.7 wt% CNF samples, their Young's modulus and fracture strain were comparable with a slight reduction for 0.7 wt% CNF. This seemed insignificantly affect the surface roughness when considering mechanical properties. Instead, the microstructure effect of 0.7 wt% CNF sample that can be seen with more CNF agglomeration found on the fracture surface of this material (Fig. 5c) was likely the reason for its higher surface roughness compared to 0.3 wt% CNF. These filler agglomerations resulted in more CNF pull-out and led to rougher machined surfaces at 0.7 wt% compared to those of 0.3 wt% material. Also, a low transition temperature of 0.7 wt% CNF material contributed to more chip adhesion and smearing on the machined surfaces that could be visually recognised from the SEM images in Fig. 13. It resulted in higher surface roughness of this material compared to 0.3 wt% CNF.

4. Conclusions

This study presents an experimental investigation of the machinability of CNF reinforced epoxy nanocomposites using micromilling tools aiming to extract the impact of cutting conditions and thermomechanical properties of workpiece material on key indicators including cutting force and surface roughness. Generally, cutting speed was the most significant factor affecting cutting force whereas FPT significantly affected surface roughness. Furthermore, the machinability of EP/CNF nanocomposites in terms of cutting force and surface roughness was significantly affected by the filler content, and consequently, the thermomechanical properties of the workpiece materials with only small addition of CNFs (from 0.3 to 1 wt%). The high sensitivity of the machinability of EP/CNF nanocomposites with changing thermomechanical properties of workpiece materials indicated a typical feature of micromachining of nanocomposites. Nanocomposite samples reinforced with a filler content of 1 wt% CNF exhibited the highest machinability performance in terms of lower cutting force and high surface finish. On the other hand, 0.1 wt% samples had the worst performance. Additionally, nanocomposite samples reinforced with CNF had lower machinability compared with the neat epoxy counterpart. For micromachining at low FPTs below MUCT, the size effect exhibited by the deterioration of the surface finish due to the ploughing effect. This phenomenon was in line with the identification of MUCT value from chip morphology analysis.

Declaration of competing interest

The authors declare that they have no known competing financial interests or personal relationships that could have appeared to influence the work reported in this paper.

References

[1] Kim YA, Hayashi T, Endo M, Dresselhaus MS. Carbon nanofibers. In: Springer handbook of nanomaterials. Springer; 2013. p. 233–62.
[2] Bal S. Experimental study of mechanical and electrical properties of carbon nanofiber/epoxy composites. Mater Des (1980–2015) 2010;31(5):2406–13.
[3] Yoon S-H, et al. Novel carbon nanofibers of high graphitization as anodic materials for lithium ion secondary batteries. Carbon 2004;42(1):21–32.
[4] Yoon S-H, et al. KOH activation of carbon nanofibers. Carbon 2004;42(8–9): 1723–9.
[5] Endo M, et al. Structural characterization of cup-stacked-type nanofibers with an entirely hollow core. Appl Phys Lett 2002;80(7):1267–9.
[6] Maruyama B, Alam K. Carbon nanotubes and nanofibers in composite materials. Sampe J 2002;38(3):59–70.
[7] Le B, Khaliq J, Huo D, Teng X, Shyha I. A review on nanocomposites. Part 1: mechanical properties. J Manuf Sci Eng 2020;142(10):100801.
[8] Jiguet S, Judelewicz M, Mischler S, Bertch A, Renaud P. Effect of filler behavior on nanocomposite SU8 photoresist for moving micro-parts. Microelectr Eng 2006;83 (4–9):1273–6.
[9] Yasa IC, Tabak AF, Yasa O, Ceylan H, Sitti M. 3D-printed microrobotic transporters with recapitulated stem cell niche for programmable and active cell delivery. Adv Funct Mater 2019;29(17):1808992.
[10] Wang Z, et al. Hybrid magnetic micropillar arrays for programmable actuation. Adv Mater 2020;32(25):2001879.
[11] Sakar MS, Steager EB, Kim DH, Kim MJ, Pappas GJ, Kumar V. Single cell manipulation using ferromagnetic composite microtransporters. Appl Phys Lett 2010;96(4):043705.
[12] Shokrieh MM, Esmkhani M, Vahedi F, Shahverdi HR. Improvement of mechanical and electrical properties of epoxy resin with carbon nanofibers. Iran Polym J 2013; 22(10):721–7.
[13] Zhu J, Wei S, Yadav A, Guo Z. Rheological behaviors and electrical conductivity of epoxy resin nanocomposites suspended with in-situ stabilized carbon nanofibers. Polymer 2010;51(12):2643–51.
[14] Quaresimin M, Schulte K, Zappalorto M, Chandrasekaran S. Toughening mechanisms in polymer nanocomposites: from experiments to modelling. Compos Sci Technol 2016;123:187–204.
[15] Al-Saleh MH, Sundararaj U. Review of the mechanical properties of carbon nanofiber/polymer composites. Compos A: Appl Sci Manuf 2011;42(12):2126–42.
[16] Zhou Y, Jeelani S, Lacy T. Experimental study on the mechanical behavior of carbon/epoxy composites with a carbon nanofiber-modified matrix. J Compos Mater 2014;48(29):3659–72.
[17] Bortz DR, Merino C, Martin-Gullon I. Carbon nanofibers enhance the fracture toughness and fatigue performance of a structural epoxy system. Compos Sci Technol 2011;71(1):31–8.
[18] Wei J, Atif R, Vo T, Inam F. Graphene nanoplatelets in epoxy system: dispersion, reaggregation, and mechanical properties of nanocomposites. J Nanomater 2015; 2015.
[19] Serenko OA, Roldughin VI, Askadskii AA, Serkova ES, Strashnov PV, Shifrina ZB. The effect of size and concentration of nanoparticles on the glass transition temperature of polymer nanocomposites. RSC Adv 2017;7(79):50113–20.
[20] Qi B, Lu S, Xiao X, Pan L, Tan F, Yu J. Enhanced thermal and mechanical properties of epoxy composites by mixing thermotropic liquid crystalline epoxy grafted graphene oxide. Exp Polym Lett 2014;8(7).
[21] Kim HJ, Han J, Son Y. Effect of a monomer composition on the mechanical properties and glass transition temperature of a waterborne polyurethane/graphene oxide and waterborne polyurethane/MWCNT nanocomposite. Polymers 2020;12(9):2013.
[22] Teng X, Huo D, Wong E, Meenashisundaram G, Gupta M. Micro-machinability of nanoparticle-reinforced Mg-based MMCs: an experimental investigation. Int J Adv Manuf Technol 2016;87(5):2165–78.
[23] Kumar MN, Mahmoodi M, TabkhPaz M, Park S, Jin X. Characterization and micro end milling of graphene nano platelet and carbon nanotube filled nanocomposites. J Mater Process Technol 2017;249:96–107.
[24] Zhang X, Ehmann KF, Yu T, Wang W. Cutting forces in micro-end-milling processes. Int J Mach Tool Manuf 2016;107:21–40.
[25] Park S, Malekian M. Mechanistic modeling and accurate measurement of micro end milling forces. CIRP Ann 2009;58(1):49–52.
[26] Jun MB, Liu X, DeVor RE, Kapoor SG. Investigation of the dynamics of microend milling—part I: model development. 2006.
[27] Mahmoodi M, Mostofa M, Jun M, Park SS. Characterization and micromilling of flow induced aligned carbon nanotube nanocomposites. J Micro Nano-Manuf 2013; 1(1).
[28] Samuel J. Fundamental study of the machinability of carbon nanotube reinforced polymer composites. University of Illinois at Urbana-Champaign; 2009.
[29] Le B, et al. Micro-end-milling of carbon nanotube reinforced epoxy nanocomposites manufactured using three roll mill technique. J Manuf Process 2021;70:307–20.
[30] Samuel J, Dikshit A, DeVor R, Kapoor S, Hsia K. Effect of carbon nanotube (CNT) loading on the thermomechanical properties and the machinability of CNT-reinforced polymer composites. J Manuf Sci Eng 2009;131(3).
[31] Ramos AC, Autenrieth H, Strauß T, Deuchert M, Hoffmeister J, Schulze V. Characterization of the transition from ploughing to cutting in micro machining and evaluation of the minimum thickness of cut. J Mater Process Technol 2012;212 (3):594–600.
[32] Wang G, Yu T, Zhou X, Guo R, Chen M, Sun Y. Material removal mechanism and microstructure fabrication of GDP during micro-milling. Int J Mech Sci 2023;240: 107946.
[33] Chen W, Sun Y, Huo D, Teng X. Modelling of the influence of tool runout on surface generation in micro milling. Chin J Mech Eng 2019;32(1):1–9.
[34] Zhang J, Feng C, Wang H, Gong Y. Analytical investigation of the micro groove surface topography by micro-milling. Micromachines 2019;10(9):582.
[35] Neto HK, Diniz AE, Pederiva R. The influence of cutting forces on surface roughness in the milling of curved hardened steel surfaces. Int J Adv Manuf Technol 2016;84(5–8):1209–18.